# Supplementary Information

## Unraveling the $CO_2$ methanation and capture ability of NiO@metal oxides

Huldah Suharika Chitturi[1†], Yalagandula Lavanya[1†], Yaddanapudi Varun[1], Anurag Ramesh[1], Sri Himaja Pamu[1], I. Sreedhar[1], Satyapaul A. Singh[1, 2 *]

[1]Department of Chemical Engineering, Birla Institute of Technology and Science (BITS) Pilani, Hyderabad Campus, Jawahar Nagar, Kapra Mandal, Hyderabad-500 078, India.

[2]Materials Centre for Sustainable Energy & Environment, Birla Institute of Technology and Science (BITS) Pilani, Hyderabad Campus, Jawahar Nagar, Kapra Mandal, Hyderabad-500 078, India.

[†] Contributed equally

*Corresponding author

Tel: +91 40 66303 566

E-mail: satyapaul@hyderabad.bits-pilani.ac.in, India.

## S.1. Materials and methods

The chemicals used for the synthesis are Nickel nitrate hexahydrate ($Ni(NO_3)_2.6H_2O$, SRL chemicals, 98 %), Cobalt nitrate hexahydrate ($Co(NO_3)_2.6H_2O$, SRL chemicals, 98%), Cerium nitrate hexahydrate ($Ce(NO_3)_3.6H_2O$, SRL chemicals, 98%), Zirconyl nitrate oxynitrate ($ZrO(NO_3)_2.xH_2O$, SRL chemicals, 98%), Tetra orthosilicate ($SiC_8H_{20}O_4$, TCI chemicals, 99%) Polyvinylpyrrolidone, PVP K-30 ($(C_6H_9NO)_n$, SRL chemicals), Ammonia solution ($NH_4OH$, 25%, SRL chemicals). For catalytic activity, the gases were procured from Chemix gases Pvt Ltd, India. The gases used are carbon dioxide ($CO_2$, 99.99%), Hydrogen ($H_2$, 99.99%), and Nitrogen ($N_2$, 99.99%).

### S.1.1. Synthesis of NiO nanoparticles using the precipitation method

In a typical synthesis, 100 mL of 0.25 M Nickel nitrate hexahydrate ($Ni(NO_3)_2.6H_2O$) was prepared initially. To this solution, 1.0 M of $NH_4OH$ solution was added dropwise until the pH reached between 9-10. After separating the solution from the precipitate, the precipitate was thoroughly washed with ethanol thrice to remove any soluble impurities. The clean precipitate was collected and kept in a hot air oven at 120°C for overnight drying. After drying, the precipitate was grinded and subjected to calcination at 400°C for 2 h in the furnace. The obtained samples were again grinded and subjected to the development of core-shell nanoparticles.

### S.1.2. Synthesis of NiO@S (S = $Co_3O_4$, $CeO_2$, $SiO_2$ and $ZrO_2$) core-shell nanoparticles using modified Stöber method

Core-shell nanoparticles were synthesized using the modified Stöber method. In brief, 0.5 g of NiO nanoparticles were added to the 100 mL ethanol solution. To this solution, 5 g of PVP K-30 was added and stirred for 10 min until a clear solution was obtained. Then 10 mL of 25% ammonia solution was added and stirred for 2 h to make NiO particles chemically interact with the polymer. After 2 h, 2.5 mL of TEOS was added to the solution and allowed to stir for 15 h. The obtained solution was filtered and washed with ethanol several times. Both synthesis steps are performed at room temperature making the entire synthesis energy efficient compared to other traditional synthesis routes. The collected sample was kept in a hot air oven at 80°C for 12 h. The dried sample was directly kept in the furnace for further calcination at 550°C for 3 h. Based on the same NiO weight ratio, the shells were interchanged with cobalt oxide, cerium oxide, and zirconia, making different core-to-shell ratio nanoparticles. Similar protocol for $NiO@SiO_2$ was employed by replacing with nitrate precursors to prepare $NiO@Co_3O_4$, $NiO@CeO_2$, and $NiO@ZrO_2$. The weights for NiO to shell precursors ($Co(NO_3)_2.6H_2O$, $Ce(NO_3)_3.6H_2O$ and $ZrO(NO_3)_2.xH_2O$) were taken in the ratio of 1:5 to follow the consistency of precursor concentrations in the synthesis. The obtained nanoparticles are denoted as $NiO@Co_3O_4$, $NiO@CeO_2$, and $NiO@ZrO_2$, respectively and further subjected to various characterization techniques.

### S.1.3. Characterization techniques

XRD patterns were acquired using XRD equipment (Rigaku, Japan) to identify the phases of the catalysts that were synthesized. This apparatus consists of a Cu Kα source, diffraction beam monochromator and operates at 40 kV with 30 mA. A scan rate of 2º/min was implemented from 10º to 90º. X-ray photoelectron microscopy, in combination with the Al-Kα source, was used so that the binding energies could be calculated (Thermo Fisher Scientific, USA). The apparatus for studying materials has a double-focusing hemispherical analyzer, a multi-element, high-transmission spectrometer input lens, and a 128-channel detector for generating higher snapshots spectroscopy. Graphitic carbon was used as a standard against which the binding energies of each one of the materials could be calibrated. FEI provided the field emission scanning electron spectroscopy (FE-SEM) that was used to get the topography of the materials. The Apero-S (USA) model, featuring a magnification range from 10× to 30000× operates at a high vacuum of 20 kV and utilizes high-resolution transmission electron microscopy (HRTEM, JOEL, JEM, 2100 P, Japan). The information on surface area and pore volume was acquired from Microtrac Bel (BEL Sorp mini II, Japan).

*In situ* FTIR spectra were obtained by using the Perkin Elmer equipment (spectrum 3, Singapore) which was coupled with the Praying mantis (Harrick Scientific, USA). The analysis was performed in the praying mantis accessory that contains a high-temperature chamber and a zinc selenide (ZnSe) window diffuse reflectance cell. A PID controller and a chiller were attached to the chamber to adjust the temperature. The catalyst was placed inside the high-temperature chamber and subjected to reduction for 1 h at $H_2$ atmosphere with a flowrate of 50 mL/min at 400˚C. After 1 h, the nitrogen was purged through the sample for 1 h at 100˚C with a flowrate of 50 mL/min and the background scan was taken. The feed gas with a composition of $CO_2$: $H_2$: $N_2$ of 10: 40: 50 mL/min was passed through the sample at each temperature in the range of 100-450˚C with 50˚C interval and the spectra were collected for every 5 min up to 45 min. The FTIR spectra were collected with 32 number of scans, 4 $cm^{-1}$ resolution in the range of 600-4000 $cm^{-1}$ with a data interval of 0.5 $cm^{-1}$. The high-pressure $CO_2$ and $H_2$ adsorption-desorption isotherms are measured in volumetric method using a High-Pressure Gas Sorption System (iSorb-HP-Win Version:3.0) of Quantachrome Instruments (Anton Paar 1900, Florida, USA) using an ultra-high purity grade adsorbate (purity: 99.999%) from Chemix specialty gases and equipment such that impurities are reduced. Helium is used as a carrier gas with at least 5 bar of pressure. The adsorption of $CO_2$ and $H_2$ experiments were carried out at pressures varying from 1 bar to 50 bar and temperature at 25°C. For each analysis, approximately 150 mg of material was loaded into the sample cell. Before starting the adsorption, the samples are degassed at 200°C for 6 h to eliminate any residual humidity with the help of a thermostatic circulator. Elemental analysis was performed by using an Inductively Coupled Plasma Optical Emission

Spectrometer (ICP-OES). The instrument was manufactured by Agilent Technologies (5110, Singapore). $H_2$-TPR, $CO_2$-TPD, and $H_2$ pulse chemisorption methods were implemented using AMI 300 model, Altamira Instruments, USA. The product gas analysis from $CO_2$-TPD studies was performed using Master 400 Quadrupole Mass Spectrometer, Altamira Instruments, USA.

**S.1.4. Catalytic activity studies**

A quartz tube reactor with a 4 mm ID was linked to a PID-controlled furnace with a catalyst loading of 200 mg. The catalyst bed length of the reactor was kept at 1 cm throughout the reaction. The catalyst was reduced with $H_2$ at 30 mL/min for 1 h at 400°C. The feed rate was set at 100 mL/min, allowing the feed ratio to be maintained at 2 vol% $CO_2$, 8 vol% $H_2$, and 90 vol% $N_2$. A moisture trap was used to avoid water vapor entry into the online gas chromatography equipped with methanator. The column temperature for gas chromatography is 40°C and the methanator temperature is 350°C. The column temperature of 40°C was chosen in order to control the separation of gases. Molecular sieve column and the Hayesep A column are used to separate the gases such as hydrogen, oxygen, and nitrogen before sending them to the detectors. Thermal conductivity detector (TCD) is used to detect $H_2$ separated in molecular sieve and Flame ionization detector (FID) is used to detect carbon dioxide, methane, and carbon monoxide that elutes from Hayesep A column after methanator. The reaction temperature was kept between 150°C and 400°C, with a 25°C interval and a GHSV of 47,760 $h^{-1}$ was maintained for all catalytic experiments. For finding the apparent activation energy, catalyst loading was changed from 50 to 200 mg. The feed rate conditions were adjusted to higher concentrations to meet the realistic conditions, and the flowrate was set to 100 mL/min with the feed ratio of 10 vol% $CO_2$, 40 vol% $H_2$, and 50 vol% $N_2$. $CO_2$ conversion and $CH_4$ selectivity were calculated under steady-state and isothermal conditions, using the formulae given below,

$$\%CO_2 \text{ conversion} = \frac{F_{[CO_2]_{in}} - F_{[CO_2]_{Out}}}{F_{[CO_2]_{in}}} \times 100 \quad \text{(E1)}$$

$$\%CH_4 \text{ selectivity} = \frac{F_{[CH_4]_{Out}}}{F_{[CH_4]_{Out}} + F_{[CO]_{Out}}} \times 100 \quad \text{(E2)}$$

Here, $F_{[CO_2]_{in}}$ is the inlet molar flowrate of $CO_2$, $F_{[CO_2]_{Out}}$ is the outlet molar flowrate of $CO_2$, $F_{[CH_4]_{Out}}$ is the outlet molar flowrate of $CH_4$ and $F_{[CO]_{Out}}$ is the outlet molar flow rate of CO.

### S.1.5. $H_2$-temperature programming reduction ($H_2$ – TPR) studies

A catalyst amount of 40 mg was loaded into a U-shaped quartz tube cell which was placed inside the high temperature furnace. The material was degassed at 150°C using 30 ml/min of Ar flow. In the reduction step, 30 mL/min of 10% $H_2$/rest Ar gas was passed through the packed catalyst while ramping the temperature. A PID controller was used to control the temperature and maintained the temperature range from 45ºC to 900ºC by increasing 10ºC/min. To the outlet of the reactor, thermal conductivity detector (TCD) equipped unit was connected and recorded the data with respect to temperature. A few control experiments were conducted to assess NiO role at 300°C under $CO_2$ and $H_2$ mixture. **Control Study 1:** A 30 mg catalyst was reduced at 400°C in $H_2$ at 30 mL/min after degassing step as mentioned before. Later, the temperature was decreased to 300°C and $CO_2$ alone was passed at 30 mL/min for 1 h to oxidize the reduced Ni. Later, the material cooled to 45ºC and degassed with Ar to remove weakly bound gas molecules, subsequently TPR step was conducted with $H_2$ to remove lattice oxygen from recreated NiO phase. All the control experiments were conducted *in situ* without ambient air exposure and the temperature range for TPR studies was 45-800ºC.

**Control Study 2:** The second control experiment was performed to evaluate the catalyst ability to recreate NiO phase in presence of 30 mL/min flow of $CO_2$ and $H_2$ mixture (at 1:4 ratio, without any inert gas as makeup, temperature = 300°C). Rest all steps were maintained as Control Study 1. The feed composition is an extreme condition than the reaction conditions maintained for catalytic activity.

### S.1.6. $CO_2$-temperature programming desorption ($CO_2$ – TPD) and $CO_2$ – TPD - MS studies

$CO_2$ temperature-programmed desorption (TPD) analysis was conducted using the Altamira AMI 300 instrument. This method aimed to probe the surface basicity of core-shell nanoparticles across varying temperatures. Additionally, $CO_2$-TPD coupled with mass spectrometry ($CO_2$-TPD-MS) was employed to identify reaction intermediates. In the experimental setup, 100 mg of catalyst was loaded into a U-shaped quartz tube cell. The catalyst underwent reduction via purging with pure $H_2$ at 400°C for 1 h, with helium serving as a carrier gas to remove excess and weakly bound $H_2$. For $CO_2$-TPD studies, pure $CO_2$ gas was introduced at a flow rate of 30 mL/min for 1 h at room temperature to adsorb onto the catalyst surface. After purging excess $CO_2$, the temperature was ramped from room temperature to 900°C at a rate of 10°C/min in the presence of the carrier gas (Helium). Subsequently, helium was flushed through the sample to remove any physisorbed $CO_2$. During $CO_2$-TPD analysis, the desorption of $CO_2$ from the material was monitored by in built TCD. After each analysis, the TCD response was calibrated to quantify the amount of $CO_2$ chemisorbed on the sample and the data

was processed to identify weak, medium and strong basic sites. In $CO_2$-TPD-MS analysis, the same procedure was followed, with a mass spectrometer (MS) detector to detect the mass-to-charge (m/z) ratio of the desorbed species.

### S.1.7. $H_2$ pulse chemisorption studies

Metal dispersion and active metal surface area were assessed using the $H_2$ pulse chemisorption technique with an Altramira instrument featuring a thermal conductivity detector. 100 mg of the sample was placed in a U-shaped quartz tube reactor. Surface contaminants were removed via a helium purge at 100°C for 30 min. The reduction step was performed with $H_2$ at 400°C for 1 h, and further helium gas was passed toward the catalyst to remove the excess hydrogen from the catalyst. For the $H_2$ pulse experiment, an $H_2$ and He gas mixture flowed into the reactor at 30 mL/min. Twenty Hydrogen pulses were administered, and gas detection was facilitated by the TCD. Within 20 pulses, the saturation was attained and TCD signal indicated no further adsorption. Once stabilized, spectra and dispersion were evaluated through calibration.

### S.1.8. Density functional theory (DFT) studies

Quantum mechanical first principles calculations were conducted using the Quantum ATK package to obtain mechanistic insights for converting $CO_2$ into methane in the presence of NiO as the catalyst surface. The role of Ni as the active sites are discussed in section 4.4.

The surface cleave tool present in the package was used to cleave out the (200) plane after relaxing the NiO unit cell. This is followed by constructing a 4×4 supercell consisting of 4 layers and 72 atoms. A vacuum space of 10 Å was introduced to prevent undesired interactions between neighboring atoms, which could arise due to the periodic boundary conditions employed in the simulation. The maximum force was limited to 0.05 eV/Å, ensuring that the atomic positions reached a stable configuration, while the energy convergence was set to 0.001 eV, guaranteeing precise energy calculations. The Perdew-Burke-Ernzerhof (GGA-PBE) functionals, which are known for their accuracy in describing the electronic structure of materials were applied for the DFT calculations.[49-51] The pristine NiO (200) supercell and atomic positions were fully relaxed by using Limited-Memory-Broyden-Fletcher-Goldfarb-Shanno (LBFGS) Quasi-Newton algorithm during geometric optimization.[52] The use of the LBFGS Quasi-Newton algorithm for geometric optimization guarantees efficient convergence to the equilibrium atomic positions, enabling reliable characterization of the catalyst surface and its interaction with reactant molecules.

Additionally, the 3×3×1 k-points mesh selected for the Brillouin zone in the Monkhorst-Pack scheme ensures adequate sampling of the reciprocal space, providing accurate electronic structure

information crucial for understanding the catalytic process.[53] This comprehensive computational approach allows for the elucidation of key mechanistic insights into the $CO_2$ to methane conversion process over NiO, facilitating the design and optimization of efficient catalyst materials.

Understanding the stability of adsorbent sites plays a crucial role in optimizing the performance of catalytic reactions. Each species involved in the reaction exhibits selectivity towards specific sites on the catalyst surface. In this study, two distinct sites, namely O-Top and Ni-Top, were selected for the stability analysis due to their significance in the catalytic process.[54-55] O-Top refers to a site where the oxygen atoms of the NiO lattice are exposed, while Ni-Top corresponds to a site where the nickel atoms are exposed. These sites offer different binding environments for adsorbates, potentially influencing the adsorption strength, activation barriers, and reaction pathways of the catalytic process. The stability of these sites was characterized by calculating the adsorption energy of all the reactants, intermediates and products adsorbed onto these sites.

$$E_{ad} = E_{ads/P} - E_{ads} - E_P \quad \text{(E3)}$$

where $E_{ads}$ is the total energy of the isolated adsorbate molecule, $E_P$ is the total energy of the isolated pristine surface, and $E_{ads/P}$ is the total energy of the adsorption system. By comparing the adsorption energies of different species on each site, valuable insights into the stability of adsorption at these sites were obtained. The results of this analysis, presented in Table S1, provide a detailed understanding of the relative stability of adsorbent sites and their impact on the catalytic performance of the system. This information serves as a crucial guide for the rational design and optimization of catalyst materials for enhanced reaction efficiency and selectivity.

## S.2. The mechanistic steps in DFT simulations

### *S.2.1 Pathway 1*

Detailed reaction mechanism of Pathway 1 that proceeds through forming formate as the intermediate species.

$$CO_2 + {}^* \longrightarrow CO_2^* \quad \text{(R1)}$$

$$H_2 + 2^* \longrightarrow 2H^* \quad \text{(R2)}$$

$$CO_2 + * + 2H^* \rightarrow HCOO^* + H^* \quad \text{(R3)}$$

$$HCOO^{*} + H^{*} \longrightarrow HCOOH^{*} \quad \text{(R4)}$$

$$H_2 + 2^{*} \longrightarrow 2H^{*} \quad \text{(R5)}$$

$$HCOOH^{*} + 2H^{*} \longrightarrow H_2COOH^{*} + H^{*} \quad \text{(R6)}$$

$$H_2COOH^{*} \longrightarrow H_2CO^{*} + H_2O^{*} \quad \text{(R7)}$$

$$H_2O^{*} \longrightarrow H_2O + {}^{*} \quad \text{(R8)}$$

$$H_2 + 2^{*} \longrightarrow 2H^{*} \quad \text{(R9)}$$

$$H_2CO^{*} + 2H^{*} \longrightarrow H_2COH^{*} + H^{*} \quad \text{(R10)}$$

$$H_2COH^{*} \longrightarrow CH_2^{*} + OH^{*} \quad \text{(R11)}$$

$$CH_2^{*} + OH^{*} + H^{*} \longrightarrow CH_2^{*} + H_2O^{*} \quad \text{(R12)}$$

$$H_2O^{*} \longrightarrow H_2O + {}^{*} \quad \text{(R13)}$$

$$H_2 + 2^{*} \longrightarrow 2H^{*} \quad \text{(R14)}$$

$$CH_2^{*} + 2H^{*} \longrightarrow CH_3^{*} + H^{*} \quad \text{(R15)}$$

$$CH_3^{*} + H^{*} \longrightarrow CH_4^{*} \quad \text{(R16)}$$

### *S.2.2 Pathway 2*

Detailed reaction mechanism of Pathway 2 that proceeds through the formation of carbon monoxide as the intermediate species.

$$CO_2 + {}^{*} \longrightarrow CO_2^{*} \quad \text{(R17)}$$

$$CO_2^{*} \longrightarrow CO^{*} + O^{*} \quad \text{(R18)}$$

$$H_2 + 2^{*} \longrightarrow 2H^{*} \quad \text{(R19)}$$

$$CO^{*} + O^{*} + 2H^{*} \longrightarrow CO^{*} + H_2O^{*} \quad \text{(R20)}$$

$$H_2O^{*} \longrightarrow H_2O + {}^{*} \quad \text{(R21)}$$

$$CO^{*} \longrightarrow C^{*} + O^{*} \quad \text{(R22)}$$

$$H_2 + 2^{*} \longrightarrow 2H^{*} \quad \text{(R23)}$$

$$C^{*} + O^{*} + 2H^{*} \longrightarrow C^{*} + OH^{*} + H^{*} \quad \text{(R24)}$$

$$C^{*} + OH^{*} + H^{*} \longrightarrow C^{*} + H_2O^{*} \quad \text{(R25)}$$

$$H_2O^* \longrightarrow H_2O + {}^*$$ (R26)

$$H_2 + 2^* \longrightarrow 2H^*$$ (R27)

$$C^* + 2H^* \longrightarrow CH^* + H^*$$ (R28)

$$CH^* + H^* \longrightarrow CH_2^*$$ (R29)

$$H_2 + 2^* \longrightarrow 2H^*$$ (R30)

$$CH_2^* + 2H^* \longrightarrow CH_3^* + H^*$$ (R31)

$$CH_3^* + H^* \longrightarrow CH_4^*$$ (R32)

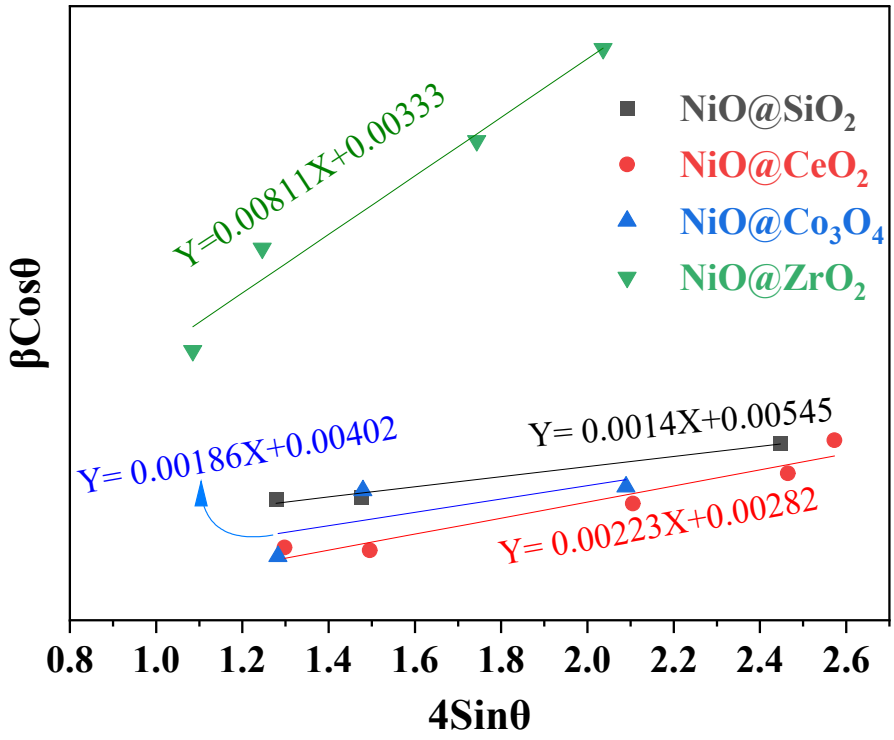


**Fig. S1** XRD patterns using Williamson-Hall equation of core-shell catalysts.

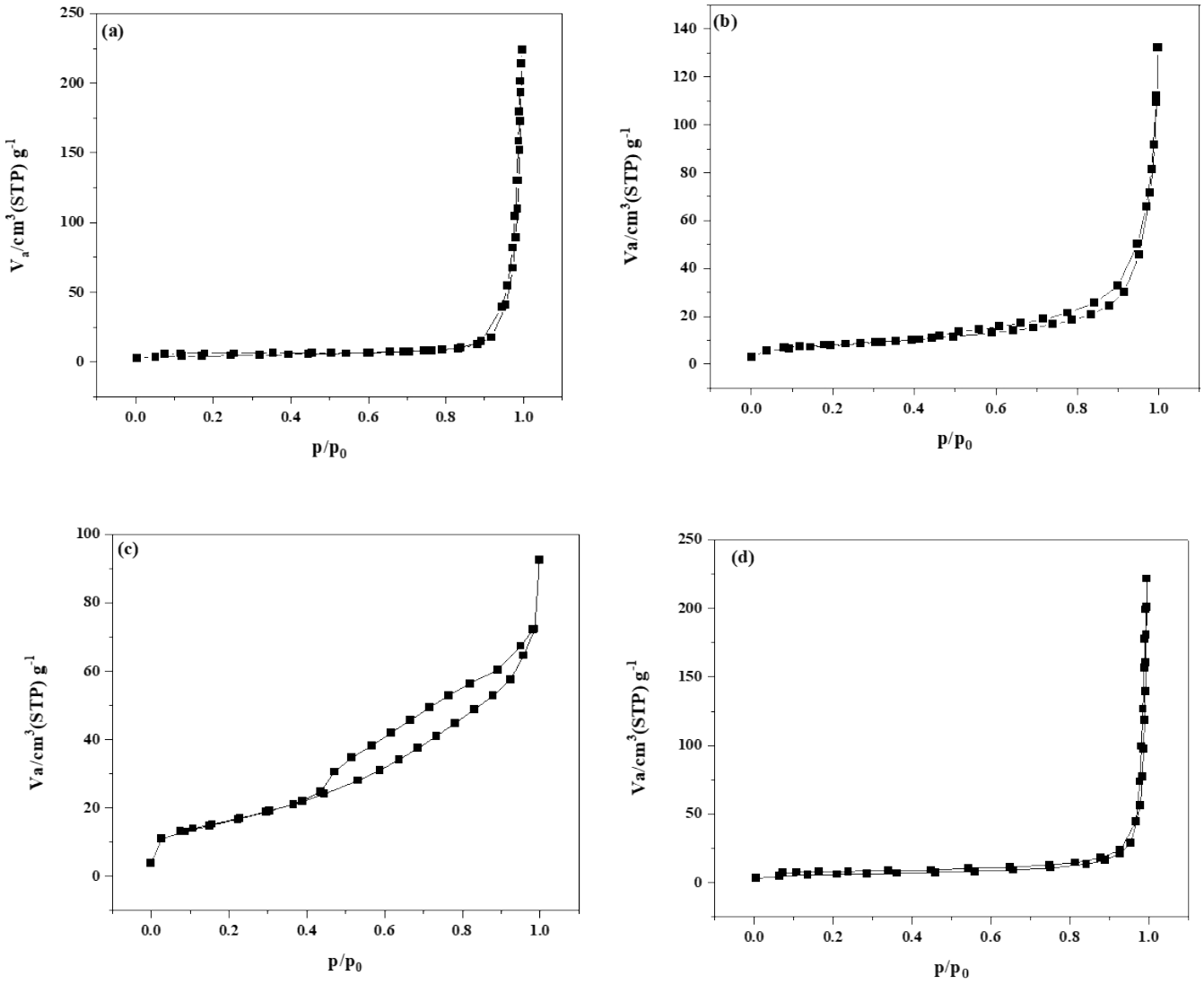


**Fig. S2** Adsorption isotherms of (a) NiO@$Co_3O_4$ (b) NiO@$CeO_2$ (c) NiO@$ZrO_2$ and (d) NiO@$SiO_2$

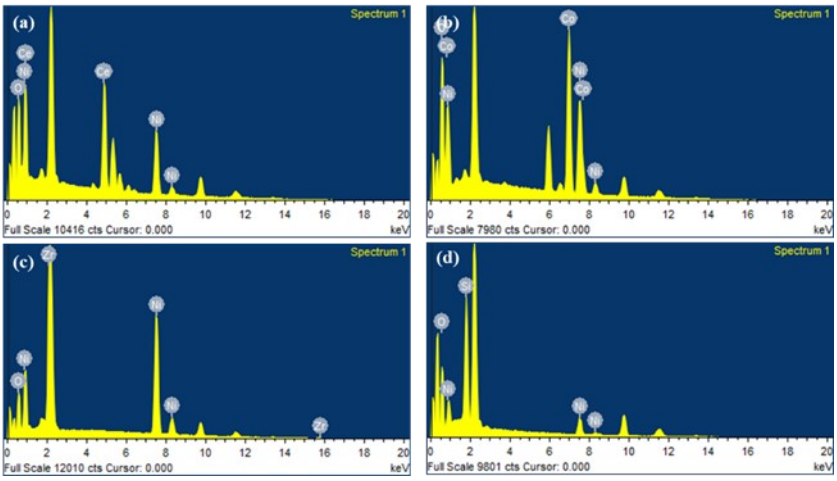


**Fig. S3** EDX images of (a) NiO@$CeO_2$ (b) NiO@$Co_3O_4$ (c) NiO@$ZrO_2$ and (d) NiO@$SiO_2$

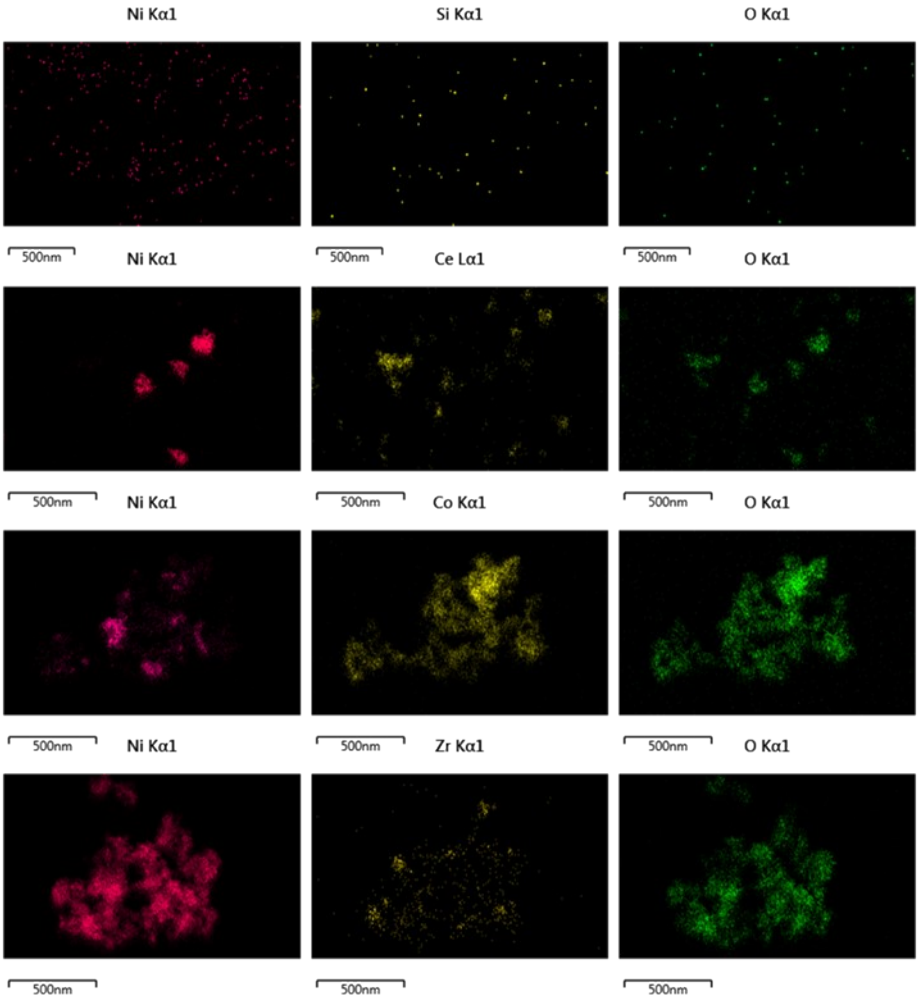


**Fig. S4** TEM based EDS mapping of elements.

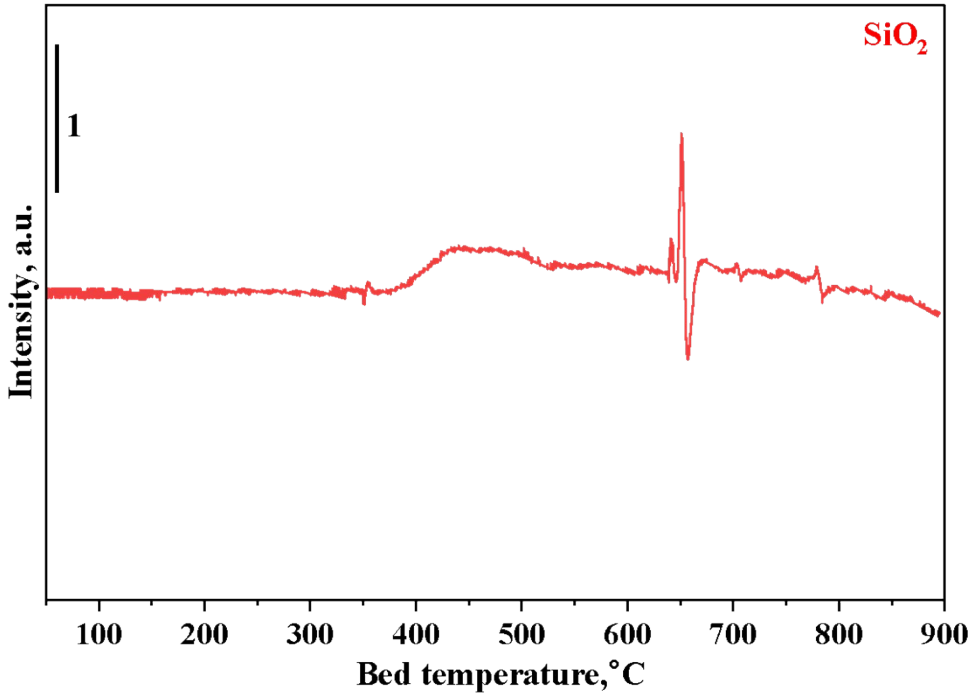


**Fig. S5** $H_2$-TPR study on $SiO_2$ catalyst.

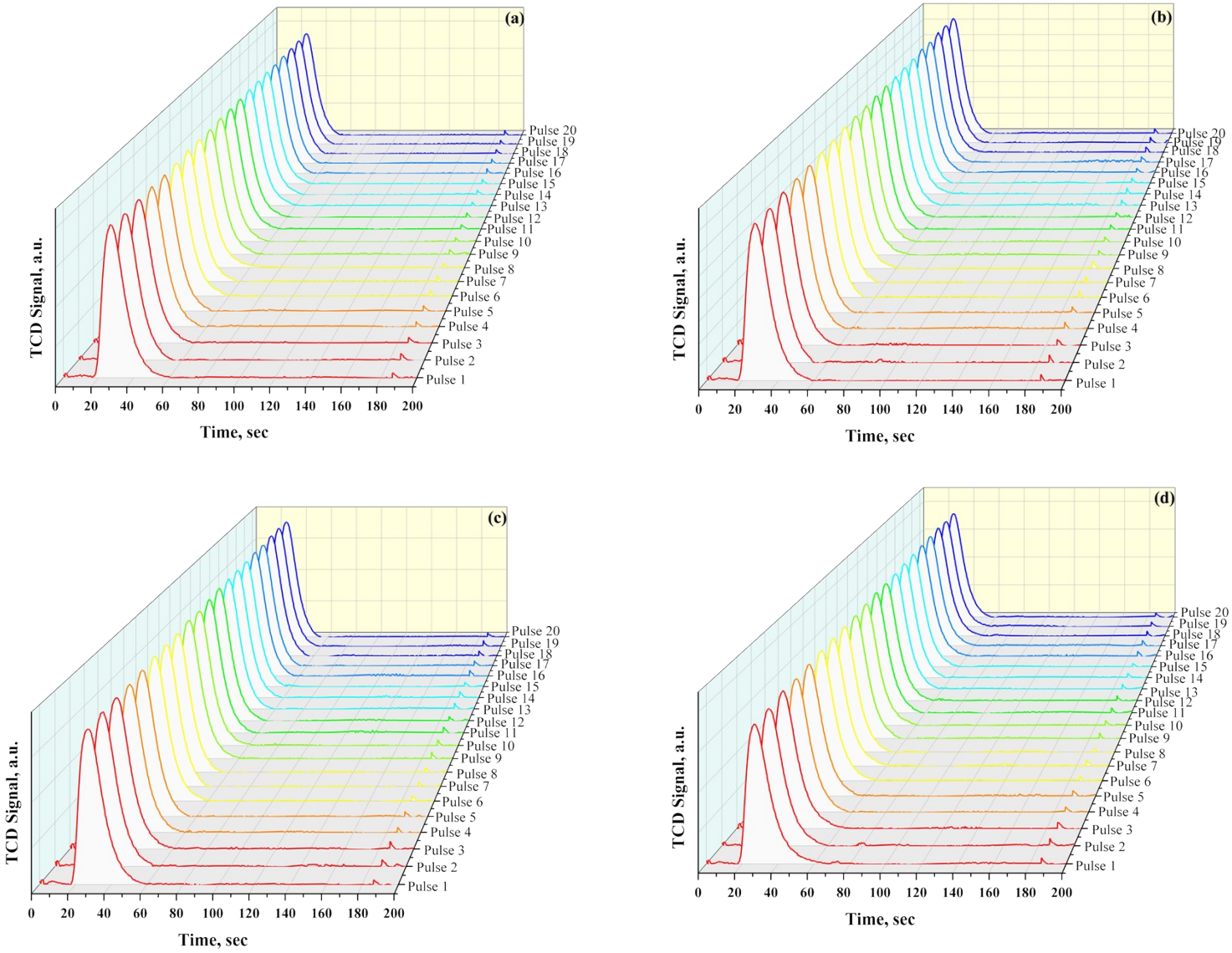


**Fig. S6** $H_2$ Pulse graphs of (a) NiO@$SiO_2$, (b) NiO@$CeO_2$, (c) NiO@$Co_3O_4$ and (d) NiO@$ZrO_2$.

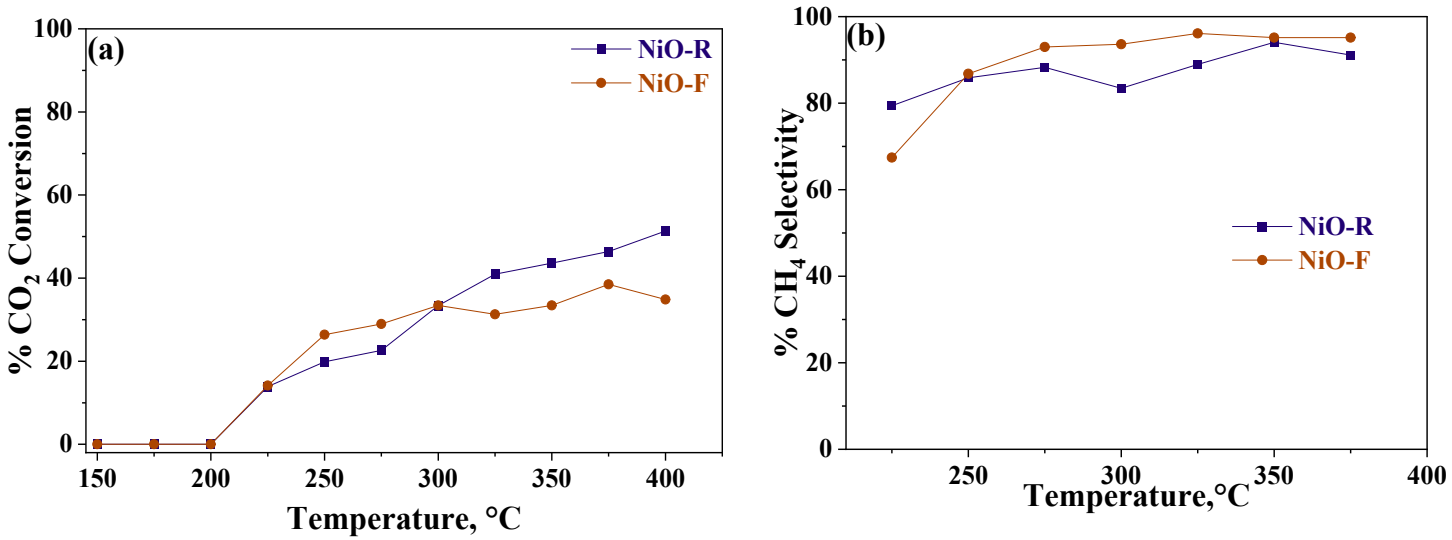


**Fig. S7** Catalytic activity studies plot (a) % $CO_2$ conversion and (b) % $CH_4$ selectivity for core catalyst NiO-F [Without Reduction], NiO-R [With Reduction].

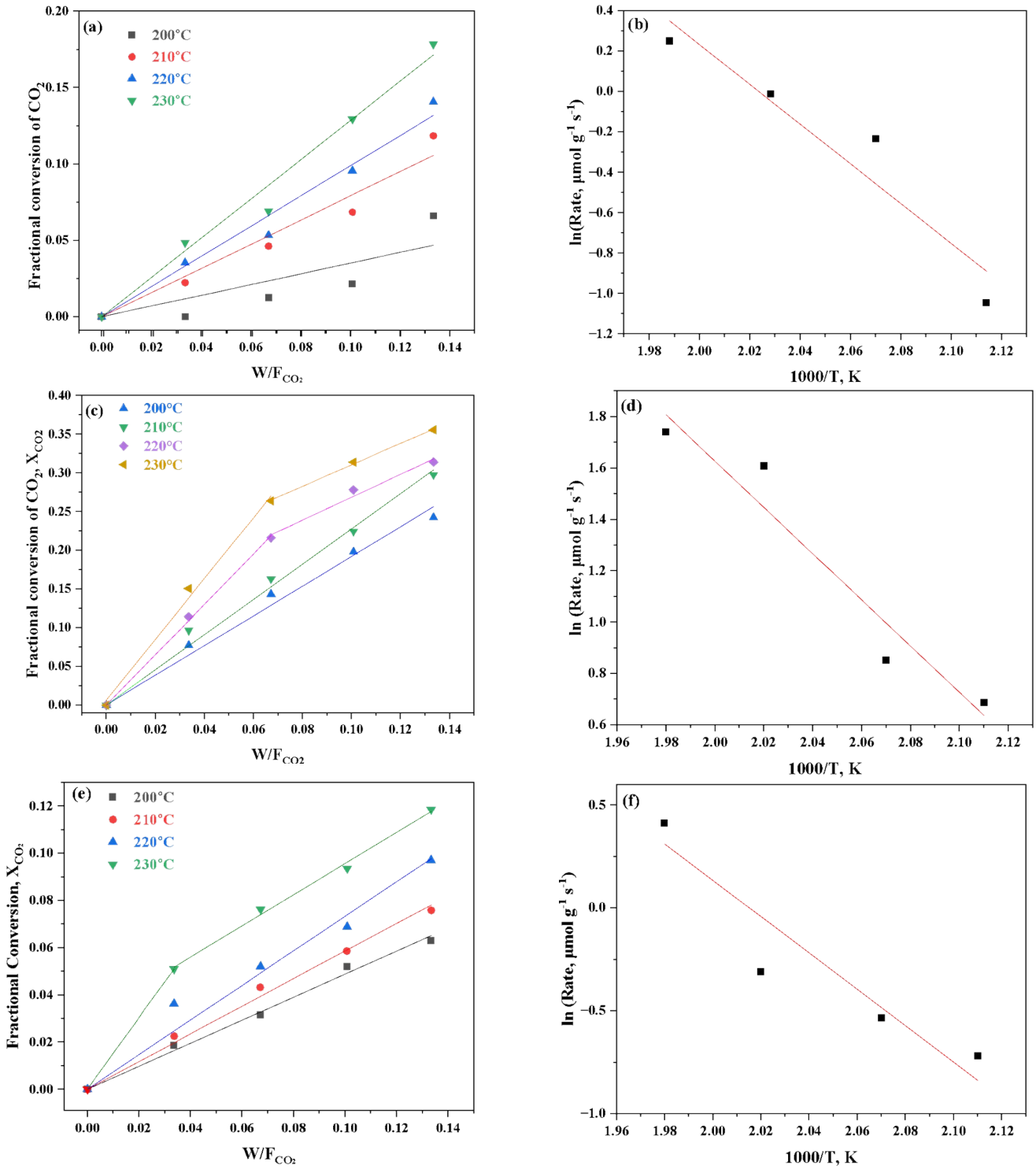


**Fig. S8** Fractional $CO_2$ conversion variation with a ratio of catalyst loading to constant molar flow rate (a) NiO@$Co_3O_4$, (c) NiO@$CeO_2$ and (e) NiO@$SiO_2$ under kinetic regime and Arrhenius plots of (b) NiO@$Co_3O_4$, (d) NiO@$CeO_2$ and (f) NiO@$SiO_2$ catalysts. ($CO_2$: $H_2$: $N_2$ = 2: 8: 90 vol%, GHSV = 47,760 $h^{-1}$)

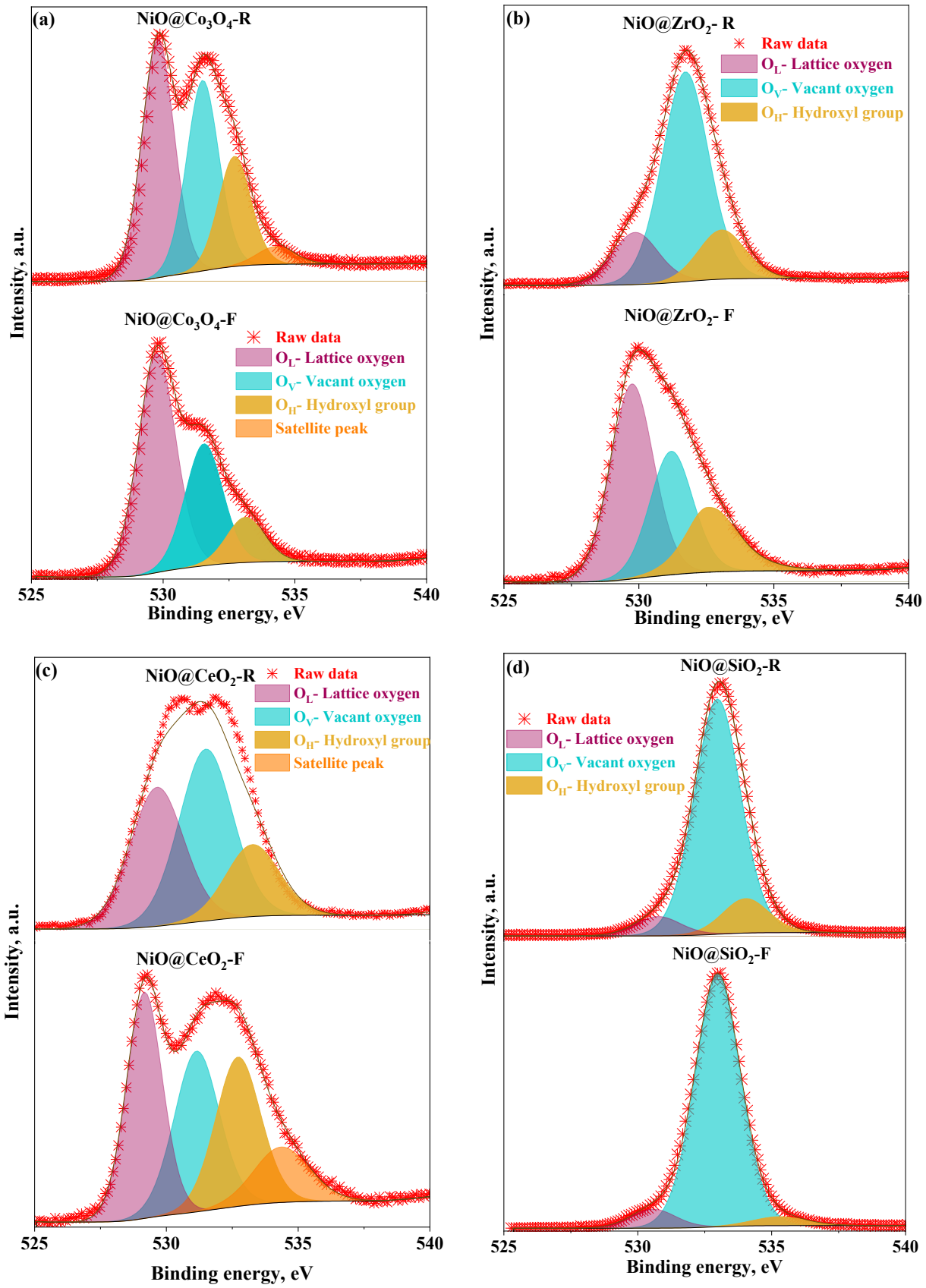


**Fig. S9** Oxygen spectra of (a) NiO@$Co_3O_4$, (b) NiO@$ZrO_2$ (c) NiO@$CeO_2$ and (d) NiO@$SiO_2$ core-shell nanoparticles

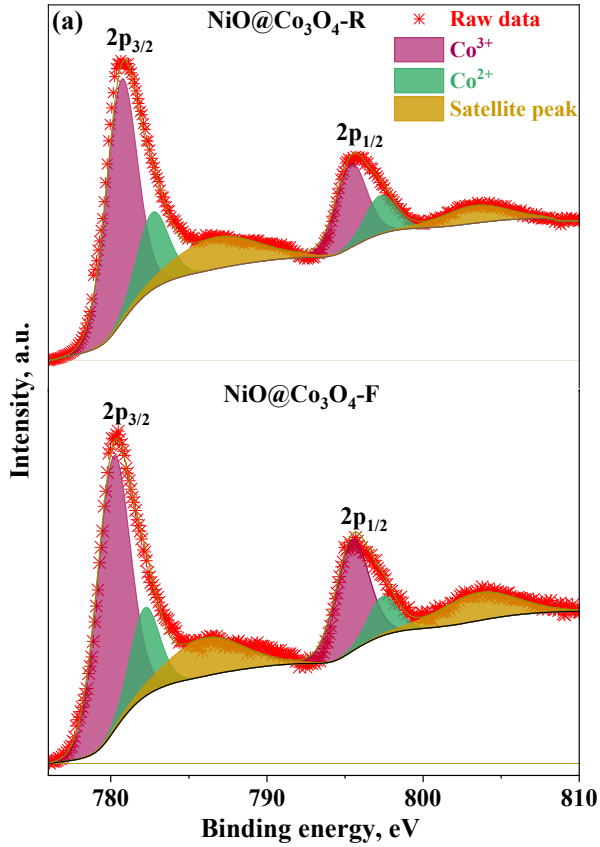
(a)
NiO@Co3O4-R
Raw data
Co3+
Co2+
Satellite peak
2p3/2
2p1/2
NiO@Co3O4-F
2p3/2
2p1/2
Intensity, a.u.
780
790
800
810
Binding energy, eV

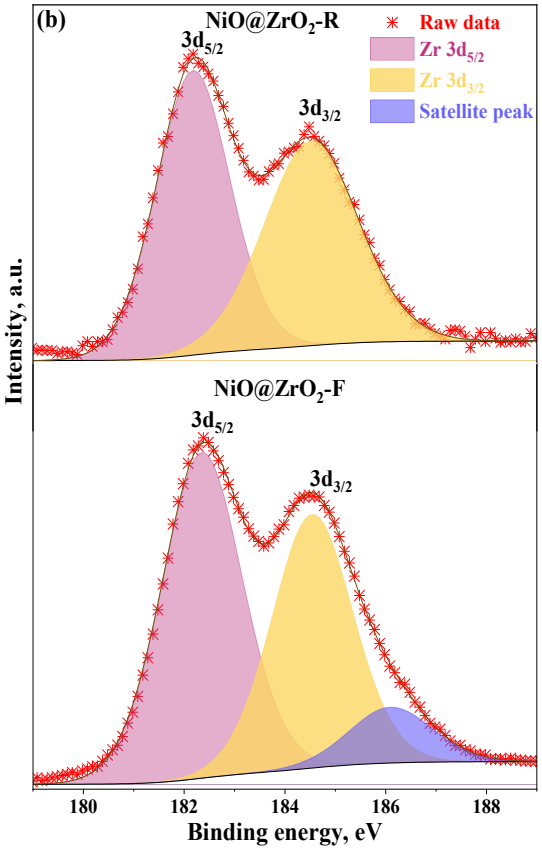
(b)
NiO@ZrO2-R
Raw data
Zr 3d5/2
Zr 3d3/2
Satellite peak
3d5/2
3d3/2
NiO@ZrO2-F
3d5/2
3d3/2
Intensity, a.u.
180
182
184
186
188
Binding energy, eV

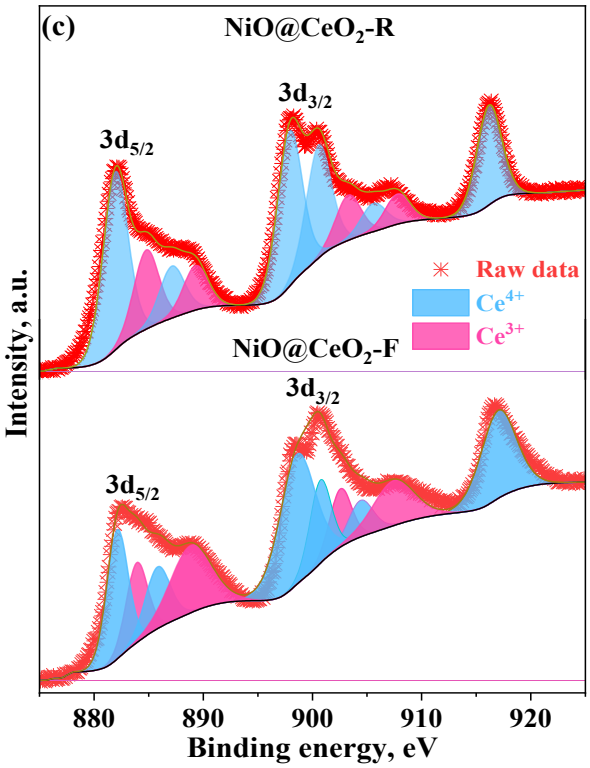
(c)
NiO@CeO2-R
3d3/2
3d5/2
Raw data
Ce4+
Ce3+
NiO@CeO2-F
3d3/2
3d5/2
Intensity, a.u.
880
890
900
910
920
Binding energy, eV

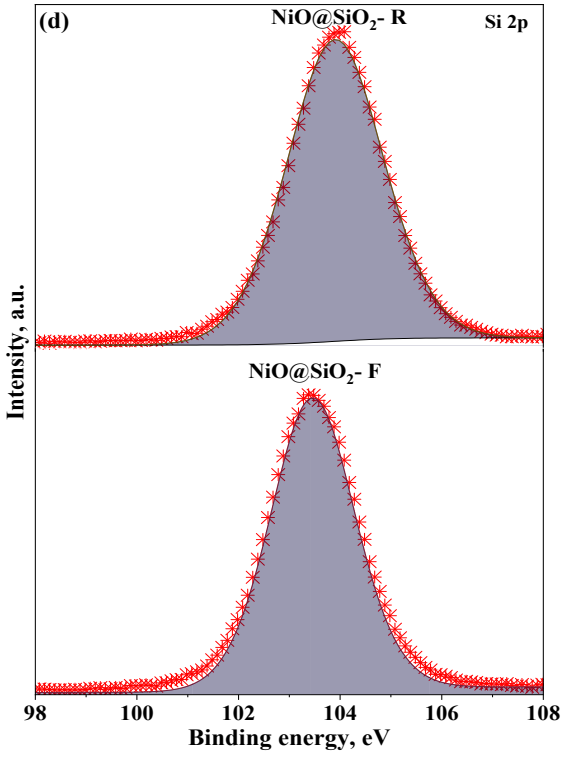
(d)
NiO@SiO2- R
Si 2p
NiO@SiO2- F
Intensity, a.u.
98
100
102
104
106
108
Binding energy, eV

**Fig. S10** Core level spectra of (a) Co 2p NiO@$Co_3O_4$, (b) Zr 3d NiO@$ZrO_2$, (c) Ce 3d NiO@$CeO_2$, (d) Si 2p NiO@$SiO_2$ for both Fresh (F) and Reduced (R) materials.

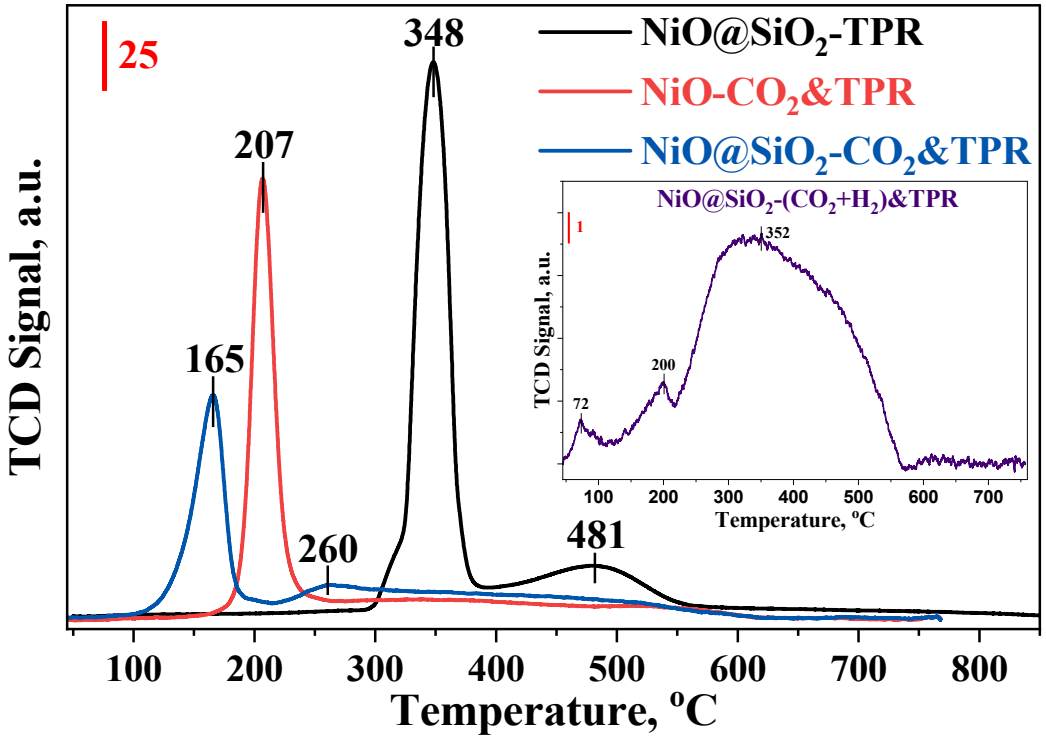


**Fig. S11** Control TPR studies on NiO, and NiO@$SiO_2$ after reoxidizing with $CO_2$, $CO_2$-$H_2$ mixture at 300°C for 1 h

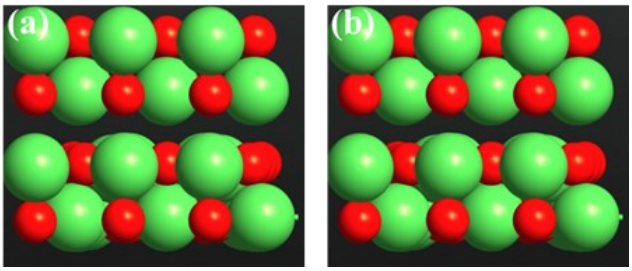


**Fig. S12** Illustration of the pristine NiO (200) lattice (a) Side view (b) Top view.

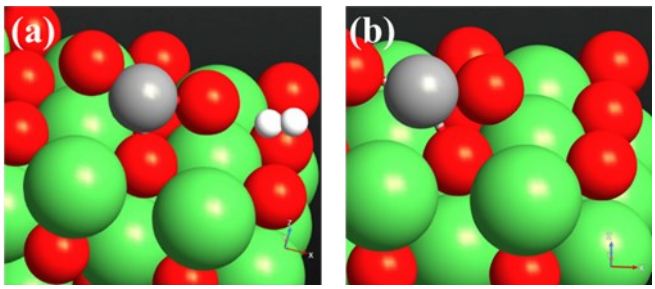


**Fig. S13** Adsorption of (a) $CO_2$ (b) $CO_2$ and 2H* on NiO (200) surface.

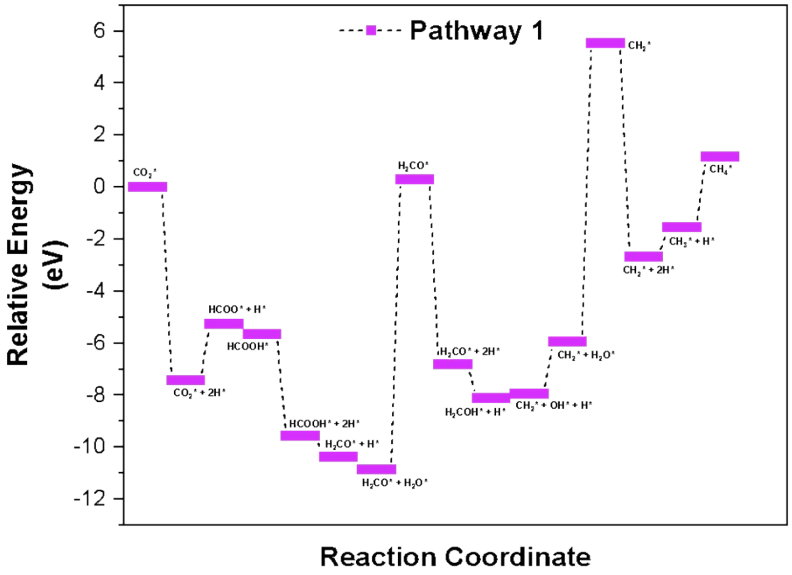


**Fig. S14** Reaction energetics for formate pathway

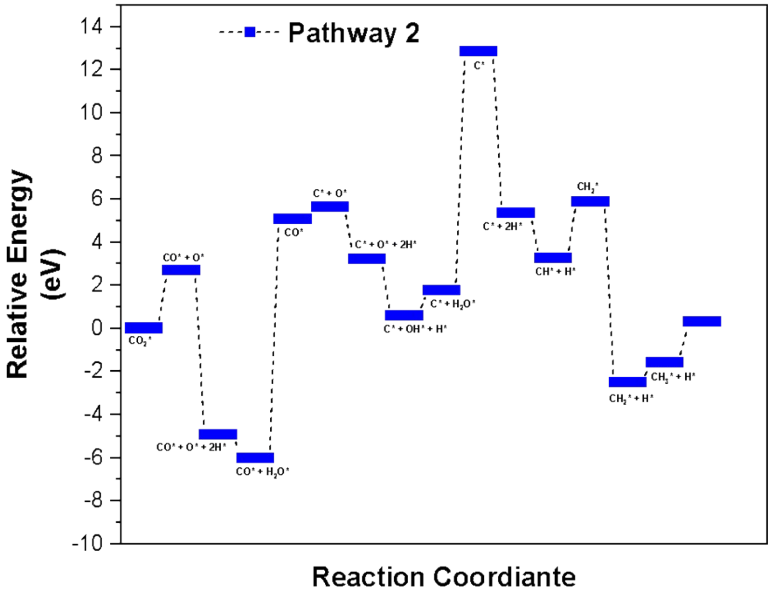


**Fig. S15** Reaction energetics for CO pathway

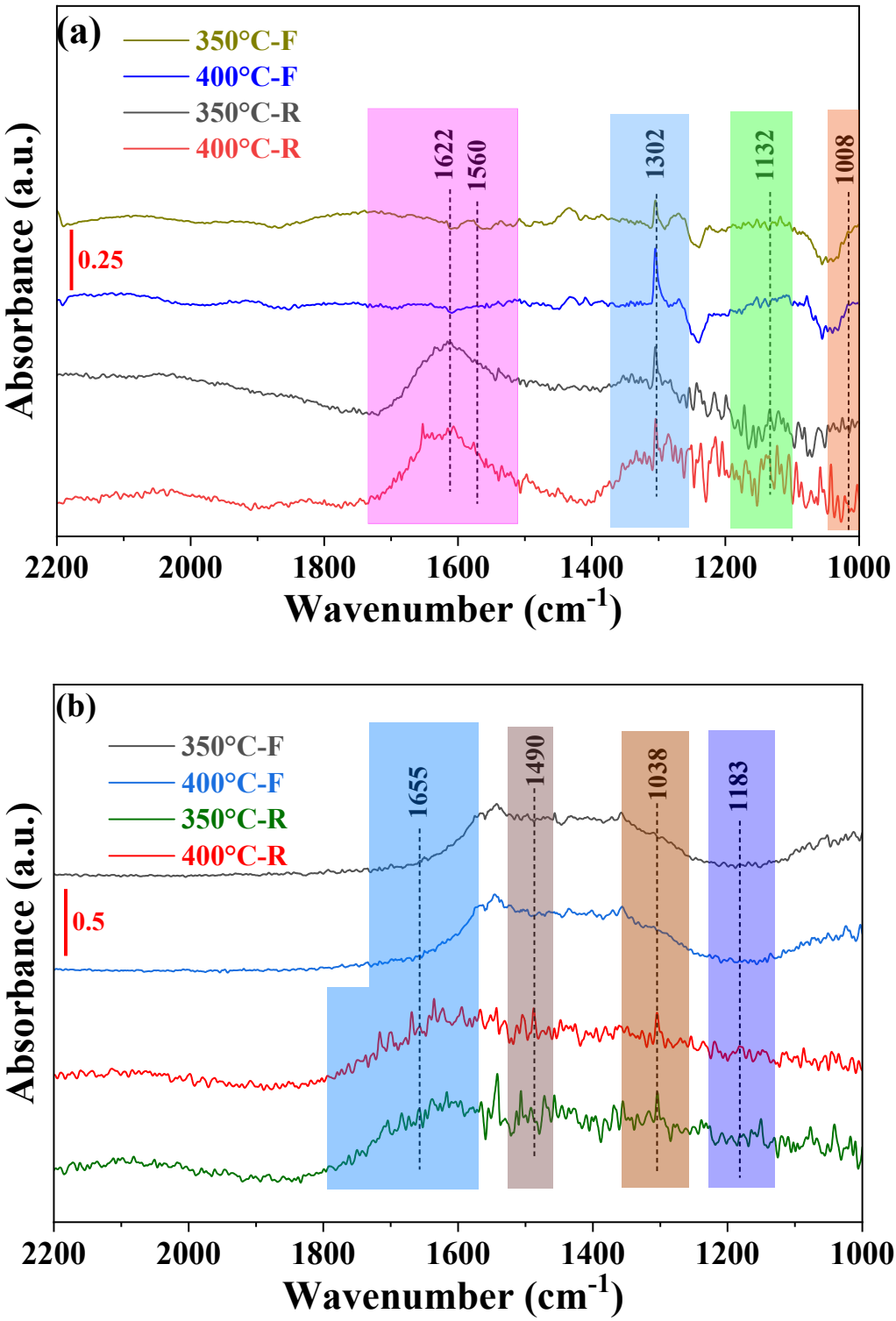


**Fig. S16** *In situ* FTIR analysis of (a) $NiO@SiO_2$ - F, R and (b) $NiO@CeO_2$ - F, R with a flowrate of $CO_2$: $H_2$: $N_2$=10: 40: 50 mL/min (R indicates catalyst with reduction at 400°C with an $H_2$ flowrate of 50 mL/min for 1 h, F indicates as synthesized catalyst).

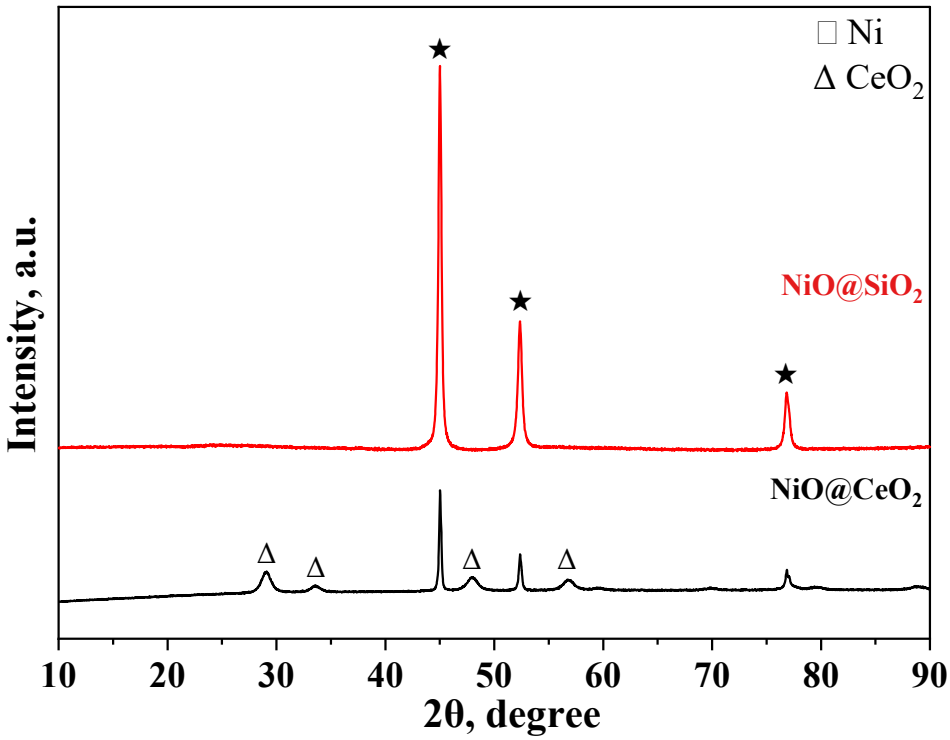


**Fig. S17** XRD of the spent catalysts.

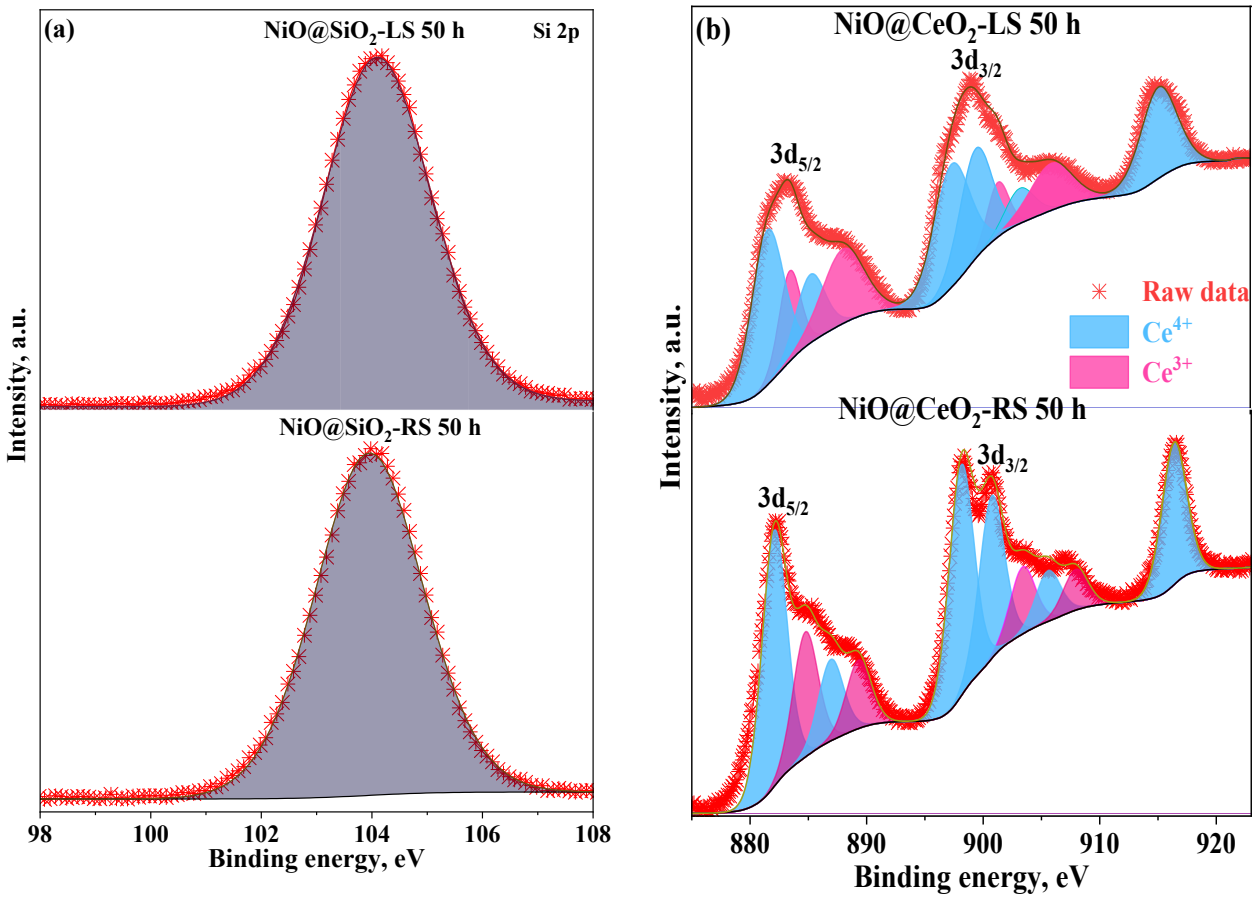


**Fig. 18** XPS spectra of (a) Si 2p NiO@$SiO_2$-50 h, and (b) Ce 3d NiO@$CeO_2$-50 h for spent catalysts under lean feed (LS) and realistic feed (RS) condition

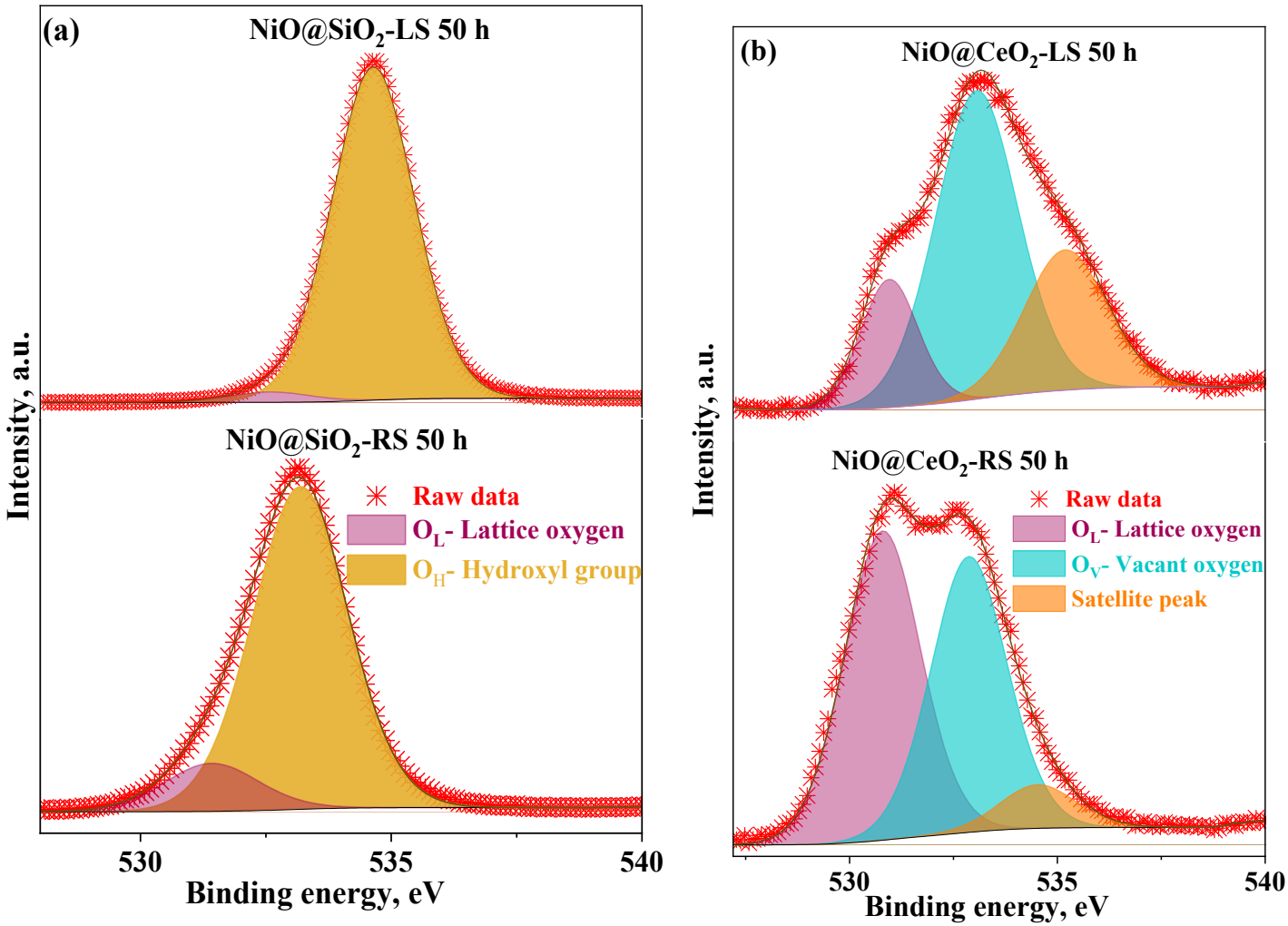


**Fig. S19** XPS of Oxygen spectra of (a) $NiO@SiO_2$ and (b) $NiO@CeO_2$ catalysts with lean and realistic stability.

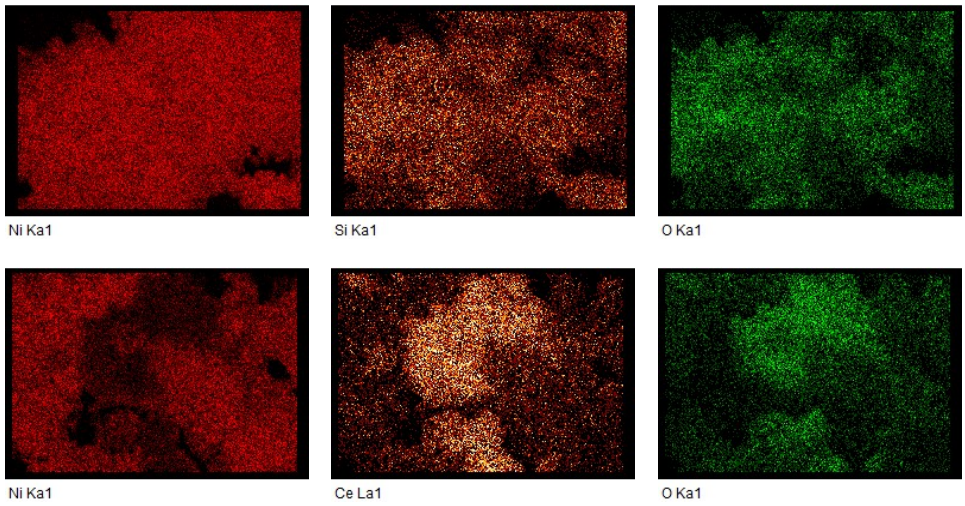


**Fig. S20** SEM based EDX mapping of elements for spent catalysts.

**Table S1.** Species vs stable sites for adsorption studies using DFT

| Species | Stable Site |
|---|---|
| $CO_2$* | O-Top |
| H* | O-Top |
| CO* | O-Top |
| HCOO* | Bridge |
| HCOOH* | Bridge |
| $H_2COOH$* | Ni-Top |
| $H_2CO$* | Bridge |
| OH* | Ni-Top |
| C* | O-Top |
| CH* | O-Top |
| $CH_2$* | O-Top |
| $CH_3$* | O-Top |
| $CH_4$* | O-Top |
| $C(OH)_2$* | O-Top |
| $CH_2O$* | O-Top |

**Table S2.** Microstrain values of core–shell catalysts.

| S. No. | Catalyst | Microstrain ($\varepsilon \times 10^{-3}$) |
|---|---|---|
| 1. | NiO@$SiO_2$ | 1.40 |
| 2. | NiO@$CeO_2$ | 2.23 |
| 3. | NiO@$Co_3O_4$ | 1.86 |
| 4. | NiO@$ZrO_2$ | 8.11 |

**Table S3.** $H_2$-Pulse Chemisorption data of fresh and reduced core-shell catalysts.

| Catalyst | % Ni dispersion | | Ni surface area, $m^2/g$ | | Number of active sites, µmol/g | |
|---|---|---|---|---|---|---|
| | Fresh catalyst (F) | Reduced catalyst (R) | Fresh catalyst (F) | Reduced catalyst (R) | Fresh catalyst (F) | Reduced catalyst (R) |
| NiO@$Co_3O_4$ | 0.80 | 0.19 | 0.02 | 0.04 | 526.13 | 661.29 |
| NiO@$CeO_2$ | 0.39 | 0.42 | 0.03 | 0.21 | 619.40 | 1579.8 |
| NiO@$ZrO_2$ | 0.36 | 0.52 | 0.03 | 0.25 | 453.88 | 1249.4 |
| NiO@$SiO_2$ | 0.41 | 0.69 | 0.06 | 0.35 | 678.03 | 1651.3 |

**Table S4.** Band edge calculation of core-shell catalysts.

| Compound | Bandgap (eV) | Electronegativity (eV) | Conduction band edge (eV) | Conduction band offset (eV) |
|---|---|---|---|---|
| NiO | 1.39 | 5.76 | 5.065 | |
| NiO@$SiO_2$ | 3.92 | 6.18 | 4.22 | 0.845 |
| NiO@$CeO_2$ | 2.6 | 5.84 | 4.54 | 0.525 |
| NiO@$Co_3O_4$ | 1.47 | 5.88 | 5.145 | -0.08 |
| NiO@$ZrO_2$ | 3.38 | 5.63 | 3.94 | 1.125 |

**Table S5.** *In situ* FTIR Spectra species table for all catalysts for $CO_2$ methanation studies.

| Species | Notations | $NiO@SiO_2$ | $NiO@CeO_2$ | $NiO@Co_3O_4$ | $NiO@ZrO_2$ |
|---|---|---|---|---|---|
| | | Wavelength ($cm^{-1}$) | | | |
| $CO_2/OH^-$ | ν (OH) | 3724-3624 | 3725-3597 | 3737-3606 | 3737-3597 |
| $CH_4$ | ν (CH) | 3013, 1302 | 3015, 1308 | 3014, 1307 | 3015, 2854 |
| $CO_2$ | ν ($CO_2$) | 2396-2241 | 2393-2224 | 2391-2227 | 2386-2230 |
| CO | ν (CO) | - | - | 2182, 2214 | 2106,2187 |
| | ν- br-CO | 1872 | - | - | - |
| Formate ($HCOO^*$) | $\nu_{as}$ ($CO_2$) | 1560 | 1490 | - | 1566 |
| $CO_2^*$-Ni | $\nu_{as}$ ($CO_2$) | - | - | - | 1758 |
| Bicarbonate ($CO_3H^*$) | $\nu_{as}$ ($CO_3$) | 1622 | - | - | - |
| | $\nu_s$ ($CO_3$) | 1008 | - | 1102 | 1068 |
| Bi-dentate carbonate | $\nu_{as}$ ($CO_3$) | - | 1655 | - | - |
| | $\nu_s$ ($CO_3$) | 1132 | - | - | 1306 |
| Monodentate carbonate | $\nu_s$ ($CO_3$) | - | - | - | 1444 |
| Carbonate | ν ($CO_3$) | - | 1183 | 1390 | - |

**Table S6.** $N_2$ adsorption-desorption analysis of the spent catalyst.

| Spent catalyst | BET surface area ($m^2/g$) | Total pore volume ($cm^3/g$) | Average pore diameter (nm) |
|---|---|---|---|
| $NiO@SiO_2$ | 46 | 0.1154 | 9.94 |
| $NiO@CeO_2$ | 27 | 0.0545 | 7.95 |